

A Biologically Interpretable Two-stage Deep Neural Network (BIT-DNN) For Hyperspectral Imagery Classification

Yue Shi, Liangxiu Han, Wenjiang Huang, Sheng Chang, Yingying Dong, Darren Dancey, Lianghao Han

Abstract—Spectral-spatial based deep learning models have recently proven to be effective in hyperspectral image (HSI) classification for various earth monitoring applications such as land cover classification and agricultural monitoring. However, due to the nature of "black-box" model representation, how to explain and interpret the learning process and the model decision remains an open problem. This study proposes an interpretable deep learning model – a biologically interpretable two-stage deep neural network (BIT-DNN), by integrating biochemical and biophysical associated information into the proposed framework, capable of achieving both high accuracy and interpretability on HSI based classification tasks. The proposed model introduces a two-stage feature learning process. In the first stage, an enhanced interpretable feature block extracts low-level spectral features associated with the biophysical and biochemical attributes of the target entities; and in the second stage, an interpretable capsule block extracts and encapsulates the high-level joint spectral-spatial features into the featured tensors representing the hierarchical structure of the biophysical and biochemical attributes of the target ground entities, which provides the model an improved performance on classification and intrinsic interpretability. We have tested and evaluated the model using two real HSI datasets for crop type recognition and crop disease recognition tasks and compared it with six state-of-the-art machine learning models. The results demonstrate that the proposed model has competitive advantages in terms of both classification accuracy and model interpretability.

Index Terms—Interpretability, Deep learning, Hyperspectral images, Classification

I. INTRODUCTION

RECENTLY, the deep learning models have been widely used for the hyperspectral image (HSI)-based earth monitoring applications, such as the land cover classification and agricultural monitoring [1], [2], and ecological management [3], [4]. However, most of existing deep learning-based approaches have difficulty in explaining biophysical and biochemical characteristics due to the black-box representation of the features extracted from the intermediate layers and the complex design of the network architectures [5], [6]. Therefore, the interpretability of the deep learning for HSI classification has become one of the most active research topics in the remote sensing community, which can enhance

and improve the robustness and accuracy of models in the earth monitoring applications from the biological perspective of the target entities [7]–[9].

Some efforts on interpretable deep learning-based models in the remote sensing field have been made [7]–[9]. Among all the explainable deep learning models for HSI classifications, the visualization of the feature representations is the most direct way to improve the interpretability [10]. This type of methods adds an additional layer to visualize the intermediate features or patterns, either maximizing the score of a given unit in a pre-trained deep learning model or inverting feature maps of an intermediate layer back to the input image [11]–[13]. For example, [14] studied the spatial distribution and significant of the output of each layer, and proposed a multilayer visualization approach to simultaneously visualize the sample distribution, the details of the subpixel level, the target units and labels hidden in the deep levels of airborne AVIRIS data and spaceborne Hyperion data. Another way to improve the interpretability of deep learning models is to construct the network architecture which can bring the network an explicit semantic meaning [10], [15]. For example, [16] proposed an unsupervised model, named as multiple-layer feature-matching generative adversarial networks (MARTA GANs), to explore and extract the representation of unlabelled data during the learning processes. In this model, a generative model was used to integrate local and global features, and a discriminative model was set to learn better spectral representations from HSI images.

Despite existing researches are encouraging, the complexity in the interaction of the ground structure and reflectance radiation of objects makes the biological interpretability of a deep learning model challenging. On one hand, unavoidable spectral-spatial perturbations and redundancies in HSI data always cause difficulty in accurately representing the features of intermediate layers [17]. On the other hand, it is hard to capture a hierarchically biological relationship among the high-level features produced by deeper layers [18].

Generally speaking, a well-designed interpretable model for HSI classification needs to deal with two issues: 1) how to extract the interpretable features that are associated with biological attributes, 2) how to represent the hierarchical structure of biophysical and biochemical attributes of the target entities. To address these issues, in this study, a biological interpretable two-stage deep neural network (BIT-DNN) model is designed to achieve an accurate classification for HSI data with a full consideration of the biophysical and biochemical basis of the

Yue Shi, Liangxiu Han, and Darren Dancey are with Department of Computing and Mathematics, Faculty of Science and Engineering, Manchester Metropolitan University, Manchester M1 5GD, UK.

Wenjiang Huang, Sheng Chang and Yingying Dong are with Key Laboratory of Digital Earth Science, Aerospace Information Research Institute, Chinese Academy of Sciences, Beijing 100094, China.

Lianghao Han is with the Tongji University, Shanghai 200092, China

target entities during the learning process, which consists of two stages. Wherein, the first stage of this model, which is designed for the extraction of the interpretable spectral features, and generation of the low-level spectral features with enhanced biophysical and biochemical representations. The second stage is designed for characterizing the biological relationship and the hierarchical structure of the high-level joint spectral-spatial features by integrating the spatial texture information with the extracted spectral features. As a result, the proposed BIT-DNN model is able to represent the biological attributes of the target entities captured by HSI data, enabling improved interpretability of decision making.

The rest of this paper is organised as follows: Section II provides an overview of related work on existing interpretable deep learning models networks for HSI image classification; Section III presents our new proposed interpretable deep neural network (BITS-DNN) for HSI image classification; Section IV introduces criteria of interpretability assessment; Section V describes the experimental evaluation; Section VI concludes the work.

II. RELATED WORK ON EXISTING INTERPRETABLE DEEP LEARNING MODELS FOR HSI IMAGE CLASSIFICATION

To evaluate the interpretability of a deep learning model fairly, the interpretable criteria are essential. Generally, for a deep learning task, interpretability should be considered in the life cycle of data science: data collection, pre-processing, data modelling, post hoc analysis [19]. The intrinsic interpretability of HSI data represents the reflection and radiation characteristics of ground entities, three interpretable criteria exist in assessing and evaluating whether a deep learning model is self-explained in HSI classification. They include 1) Pre-model interpretability, 2) In-model interpretability, and 3) Post-model interpretability (post hoc analysis).

Specifically, the pre-model interpretability, which is prior to the main model construction stage, mainly focuses on enhancing the biological attributes of the ground entities hidden in the HSI data. Two of the popular approaches in pre-model interpretability are data description standardization and explainable feature enhancement. For example, [20] proposed a dimensionality reduction method to explore the spectral and spatial characteristics of HSI data, this approach improved the representation of the hyperspectral patch alignment in the main model, and performed well in the small sample learning. [21] transformed original three colour channels into an interpretable dataset with a tensor representing the potential shapes or texture attributes of target objectives.

The in-model interpretability refers to use the causality or physical constraints on the main model and enable them to extract interpretable features with explicit semantic meaning. [22] developed a deep capsule CNN-based network for HSI classification tasks in order to better model the hierarchical relationships of features. Through the exploitation of the correlation of spectral-spatial features, the approach added structures called capsules to the CNN network. The capsules allowed efficient handling of high level complexity of the entities, including the spatial position in the image, the associated spectral

signatures, and the potential transformations. Although such approaches can improve the interpretability, they could always make the network layers deeper. Thus, a significant number of filters are added into the network architecture, leading to the vanishing gradients problem and the limited performance of activations and gradients in the training progress [23], [24]. From this aspect, the priori knowledge-based feature enhancement or encoding technology is an efficient way to uncover the discriminate spectral-spatial characteristics hidden in the raw hyperspectral images [25]. For instance, in order to formalize and exploit the knowledge of automatic urban objects identification, [26] proposed a knowledge-based deep learning model for urban object detection. In comparison with traditional CNN-based approaches, this model provided a better performance on the interpretation of HSR images in order to map the territory automatically. [27] proposed an LiDAR-based deep learning model to classify the forested landslides, in which the prior-knowledge was manually integrated with the feature extraction layers. As a result, the output features from the intermediate layers provided interpretable information for the geological characteristics of the target landslide, which subsequently achieved a better forested landslide classification in steep and rugged terrain.

The post-model interpretability, which is generally decoupled from the main model, refers to explain the representations of the intermediate outputs. Two of the popular post-model interpretability approaches include: the visualization-based approach and the interpretable activation optimization. For example, the visualization-based approach is the most direct way to explore the high-level representations of the spectral information hidden in the deeper layers. [11] compared these two different ways for extracting and visualizing image features from different layers and encoding dense features at multiple scales into global features. Since [28] introduced a principle component analysis based activation function for optimizing the deep spectral-spatial features collected from the HSI classification framework, various convolutional neural network (CNN) based deep learning models have been focused on the exploration and interpretation of the spectral-spatial pattern of the target entities using the post-interpretable approach. For instance, [29] concatenated the pixel-wised spectral-spatial features and the visualized full connected layers to extract and explain the contributions and representations of the intermediate outputs for the final classification. [12] explored the interpretation of the training process in an unsupervised way, for this purpose, they proposed an encoder-decoder paradigm, in which the significant information of the input HSI patches was extracted in a lower dimensional space via a CNN encoder.

However, most of the existing interpretable deep learning approaches were designed based on the statistical properties of the sample space [30], [31]. Thus, the learning process is modelled as a set of joint probability density functions, and a large number of high-quality labelled training data is required. Neglecting the biophysical and biochemical attributes hidden in the redundancy information of the HSI data makes the classification performance highly depend on the scale and quality of the labelled samples. Moreover, the effect of mixed-pixels,

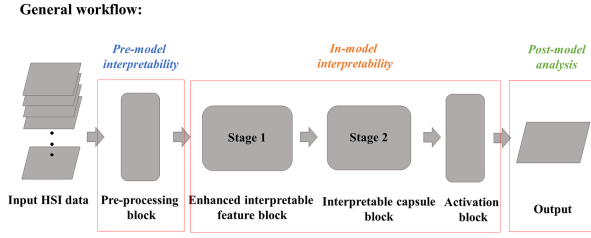


Fig. 1. The high-level system overview of the proposed interpretable two-stage spectral-spatial deep neural network

which may degrade the intra-class variability, exaggerate the inter-class similarity and produce feature interferences during the learning process, were often not fully considered [32], [33]. Therefore, most existing deep learning approaches are often have a poor interpretability for the high-level features of HSI data and the salt and pepper noises on the final classifications [34].

III. THE PROPOSED METHOD: A BIOLOGICALLY INTERPRETABLE TWO-STAGE DEEP NEURAL NETWORK (BIT-DNN)

In this study, we consider HSI data as a data cube X (with a size of $H \times W \times B$), where H , W , and B is the height, width, and bands of the original data cube, each pixel comprises an individual spectral signal with B bands. We propose a novel deep learning framework, a biologically interpretable two-stage deep neural network (BITS-DNN) to deal with the HSI classification. The architecture of the BIT-DNN is shown in Fig.1.

A. The pre-processing block

Considering the explicit biochemical and biophysical properties of vegetation in different band ranges [35], [36], we split HSI images into 7 segmentations: blue ($< 515nm$), green ($515 - 600nm$), red ($600 - 680nm$), red-edge1 ($680 - 710nm$), red-edge2 ($710 - 750nm$), red-edge3 ($750 - 790nm$), near infrared ($> 790nm$). The process in each data segmentation is parallel, which not only increases the computing efficiency, but also help interpret the photochemical meaning of the intermediate variables.

B. Stage 1– An enhanced interpretable feature block

The enhanced interpretable feature block, the first stage of feature learning, is introduced to extract and generate interpretable low-level spectral features. It consists of multiple layers including: two *1D CNN* layers, two *fully connected* layers, and the *spectral enhanced interpretable layer*. Its architecture is shown in Fig.2.

The output of the pre-processing block is a series of HSI segmentations, and each HSI segmentation is then separately introduced into two *1D-CNN* layers of the enhanced interpretable feature block. Each of the channel works as a spectral feature extractor to learn the corresponding spectral responses

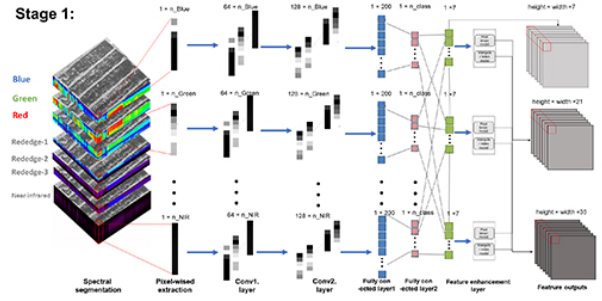


Fig. 2. The architecture of the enhanced interpretable feature block in the two-stage learning process, Stage 1. This stage is to extract and generate interpretable low-level spectral features.

which are sensitive to certain biophysical or biochemical attributes of the target class. Subsequently, two *fully connected layers* are used to map the sensitive spectral features into the corresponding classes. Finally, in order to highlight the relevance among these spectral features, a *feature enhanced interpretable layer* is designed to generate a new spectral feature set with the improved biochemical and biophysical meanings. The detailed information about each layer in this block is described in the following subsections.

1) *1D CNN layer*: For a given HSI segmentation, the spectral sub-regions which are sensitive to the target classes should be firstly separated from the redundant band information. For this purpose, two *1D CNN* layers (i.e. *conv1* and *conv2* layer in Fig.2) are introduced into our network to extract the pixel-wised spectral response features that are sensitive to the target classes from a series of filters with various reception fields. The convolution unit transforms the input vector into the aimed receptive fields as follow:

$$C_p^j = \sum_{l=1}^{rm} W_{p,l}^j I_{p,p+l-1} \quad (1)$$

where rm is the length of the receptive field, C_p^j is the layer output of the p^{th} neuron in the j^{th} filter, $W_{p,l}^j$ is the weighted factor of the p^{th} neuron in j^{th} filter for the spectral vector of the l^{th} pixel, and $I_{p,p+l-1}$ is the input spectral vector patch corresponding to the p^{th} neuron.

2) *A fully connected layer*: The output from the *conv2* is served as an input for the fully connected layer. The output, denoted as X_{out}^1 , is a 7-channel $H \times W$ dimensional matrix (i.e. $X_{out}^1 \in R^{H \times W \times 7}$) which represents the contribution of a given spectral segmentation to the targeted classes. It is noteworthy that two fully connected layers are used in our model to nonlinearly map the sensitive spectral information into a class.

3) *Spectral enhanced layer*: In order to enhance potential biophysical and biochemical information hidden in spectral information extracted from different spectral segmentations, a spectral enhanced layer is designed to considers the potential combinations of two bands and three bands in order to generate the enhanced spectral features. For two-band-combined features, denoted as X_{out}^2 , a binary model is employed as

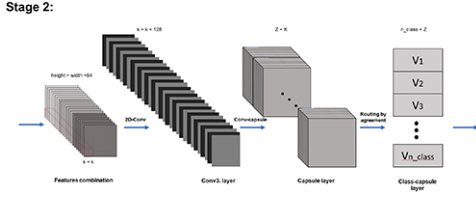


Fig. 3. The architecture of the interpretable capsule block in the two-stage learning processing, Stage 2. This stage is designed to better model the hierarchical structure of the biophysical and biochemical attributes of the target ground entities in order to achieve high accuracy and interpretability.

follow:

$$X_{out}^{2,k} = \frac{X_{out}^{1,i} - X_{out}^{1,j}}{X_{out}^{1,i} + X_{out}^{1,j}} \quad i \neq j \in [1, 7] \quad (2)$$

where, $X_{out}^{2,k}$ is the k^{th} two-band-combined feature in X_{out}^2 , k equals to $C_7^2 = 21$, thus, a total of 21 features would be generated in the feature set, X_{out}^2 .

For three-band-combined features denoted as X_{out}^3 , considering the area of a hypothetical triangle in X_{out}^1 feature space that connects the spectral information among various segmentations in a geometrical way, a triangular index model is used as follow:

$$X_{out}^{2,k} = \frac{|j-h| \times X_{out}^{1,i} - X_{out}^{1,h} - |i-h| \times X_{out}^{1,j} - X_{out}^{1,h}}{2} \quad (3)$$

$$i \neq j \in [1, 7]$$

where, $X_{out}^{3,k}$ is the k^{th} three-band-combined feature in X_{out}^3 , k equals to $C_7^3 = 35$, thus, a total of 35 features would be generated in the feature set X_{out}^2 .

Finally, the output of the enhanced interpretable feature block, denoted as X_{out} , would be a 63-channel $H \times W$ dimensional matrix, which involves a series of the extracted and generated features, thus, $X_{out} = [X_{out}^1, X_{out}^2, X_{out}^3]$.

C. Stage 2 – An interpretable capsule block

The interpretable capsule block, the second stage of feature learning, is introduced to better model the hierarchical structure of the biophysical and biochemical attributes of the target ground entities in order to achieve highly accurate classification and high interpretability. It consists of a 2D CNN layer, a capsule layer and a classification capsule layer (see Fig.3). Specifically, the output from the enhanced interpretable feature block (Stage 1) would be firstly input into a 2D CNN layer, in which the spatial texture information provided by the spectral feature maps are integrated into the featured spectral information and then the jointly spectral-spatial features are outputted. Subsequently, the spectral-spatial feature maps would be fed into a capsule layer, where the spectral-spatial features would be encapsulated into a series of featured tensor as high-level features. Finally, in order to use these high-level features to classify the HSI data into different classes, a class capsule layer is designed to output a membership that a certain featured tensor belongs to a label. The detailed information about the layers in the block is described in the following subsections:

1) *2D-CNN layer*: In order to integrate the spatial texture information from the neighbour pixels into the spectral features of the central pixel from the enhanced interpretable feature block, a typical *2D-CNN layer* is firstly introduced. The goal of this layer is to generate joint spectral-spatial features from the enhanced spectral features produced in Stage 1. In other words, the convolutional operation can be regarded as a feature updating process, which integrates the spatial structural information into the pixel-wised spectral feature and improves the representation of the input features for the target classes. In this layer, the input is the output spectral feature set $X_{out} \in R^{H \times W \times 63}$ from Stage 1, and then, a convolution kernel with a size of $k \times k \times q$ is employed, where $q = 63$, which considers the pixel-wised spectral features in different wavelengths. Then, a batch normalization and ReLU activation function are used to obtain the K -dimensional feature channels, $X_{out}^2 \in R^{H \times W \times K}$, with a size of $H \times W$.

2) *Capsule layers*: The traditional convolutional layers for deep neural networks might not be efficient in modelling the hierarchical structure of the extracted spectral-spatial features in a HSI classification task. This may result in a poor performance in characterizing and detecting the potential transformation and rotation of target classes. The design of the capsule layer in our approach aims to integrate the spectral-spatial scalar features into the vector features to represent the hierarchical structure of such extracted biophysical and biochemical-associated information, which provides the most comprehensive and accurate features that support the interpretability and reliability of the model.

Specifically, the capsule layer (the major capsule layer) comprises Z capsules, each of the capsules is composed of K convolutional neurons with a kernel of $k \times k \times h$. Within this layer, each capsule is able to model the hierarchical structure of the joint spectral-spatial features, X_{out}^2 , representing various attributes of target entities, such as orientation, pose, biochemical or biophysical components into a series of featured tensor. These encapsulated tensors are versatile in representing the homogeneous attributes of the targeted entities from the diversity of the spectral signatures in the HSI data, In addition, these featured tensors preserve much more information of biophysical and biochemical correlation relationships between the extracted spectral-spatial features and the targeted entities.

Compared with the general capsule layer rendered in computer vision with a series of pre-defined instantiation parameters [22], the capsule layer in our network is considered as an inverse rendering, which focuses on the extraction and detection of the instantiation parameters of the spectral-spatial feature vectors. Specifically, this inverse rendering process firstly extracts the low-level spectral-spatial information (i.e. the output of *cov3* layer), and then groups them into a four-dimensional tensor that comprises Z feature capsules with a size of $H \times W$. Each feature integrated into the tensor plays as an activity element of a linear subspace, which preserves most of the biophysical or biochemical variance (or fluctuation) information of a given class. These groups of spectral-spatial features allow the k^{th} capsule not only to detect the specific biophysical and biochemical features but also to learn the potential variants caused by the surface

structure and texture, providing the network with rotational invariance properties. In this context, the norm of an activity vector represents the instantiation parameters, and its length represents the probability of a spectral-spatial feature that the capsule is looking for. For better representation of these properties, a non-linear squash function is used in this study to scale down the length of the activity vector, $u_m^{(l)}$. The squash function is formulated as follow:

$$\check{u}_m^{(l)} = \frac{\|u_m^{(l)}\|^2}{1 + \|u_m^{(l)}\|^2} \cdot \frac{u_m^{(l)}}{\|u_m^{(l)}\|} \quad (4)$$

where $\check{u}_m^{(l)}$ is the scaled activity vector.

3) *Class-capsule layer*: The class-capsule layer is designed to connect all the outputs of Z capsules as the encoder units of targeted objectives. In this work, the length of the final encoder units is the number of classes, and the width of which is the number of the capsules (i.e. Z). For each input patch, the activity vectors will be encoded as the probability of belonging to corresponding classes. For this purpose, a dynamic routing algorithm proposed by [37] is employed to connect the current layer with the previous capsule layer in order to iteratively update the parameters between these two layers. The aim of this step is to provide a well-designed learning process that not only connects the spectral information between capsules but also highlights the part-whole spatial correlation through reinforcing the connection coefficients between different layers, and subsequently achieving accurate predictions. Mathematically, the encoder unit $\hat{u}_{n|m}^{(l)}$ in layer l is formulated as:

$$\hat{u}_{n|m}^{(l)} = W_{m,n}^{(l)} \cdot \check{u}_m^{(l-1)} + B_n^{(l)} \quad (5)$$

where $\check{u}_m^{(l-1)}$ is the m^{th} capsule outputs in layer $l-1$, $B_n^{(l)}$ is the biases of the n^{th} capsule in layer l , and $W_{m,n}^{(l)}$ is a transformation matrix that connects the m^{th} capsule output in layer $l-1$ with the n^{th} capsule output in layer l . This formula allows the low-level capsules in layer $l-1$ to make prediction for superior capsules in layer l , improving the representativeness of the extracted features in biochemical-biophysical domain. Subsequently, a dynamic routing coefficient $c_{m,n}^{(l)}$ is introduced to reinforce the prediction agreement during the process of calculating the input $s_n^{(l)}$ of capsule n in layer l :

$$s_n^{(l)} = \sum_m^{z^{l-1}} C \cdot \hat{u}_{n|m}^{(l)} \quad (6)$$

where $c_{m,n}^{(l)}$ measures the contribution of the m^{th} capsule in layer $l-1$ to activate the n^{th} capsule in layer l , the sum of all the routing coefficient $c_{m,n}^{(l)}$ must be 1, and $c_{m,n}^{(l)}$ is obtained by:

$$c_{m,n}^{(l)} = \frac{e^{b_{m,n}}}{\sum_i^{z^{(l)}} e^{b_{m,i}}} \quad (7)$$

where $b_{m,n}$ is the *log* prior which indicates the correlation relationship between the m^{th} capsule in layer $l-1$ and the n^{th} capsule in layer l , it is initialized as 0 and is iteratively refined as follow:

$$b_{m,n}^l = b_{m,n}^{l-1} + v_n^{l-1} \cdot \hat{u}_{n|m}^{(l-1)} \quad (8)$$

where v_n^l is the activity vector of the capsule layer l , which can be calculated based on the function as follows:

$$v_n^l = \frac{\|s_n^{(l)}\|^2}{1 + \|s_n^{(l)}\|^2} \cdot \frac{s_n^{(l)}}{\|s_n^{(l)}\|} \quad (9)$$

Conceptually, through the dynamic routing algorithm, the similar prediction from the capsule layer will be grouped, and subsequently capturing the robust prediction with clearer biochemical and biophysical meaning. Finally, the prediction performance can be calculated by the loss function (L) as follows:

$$L_{margin} = \sum_i^{n_{class}} T_i \max(0, edge^+ - \|v_n^l\|^2) + \mu(1 - T_i)(\max(0, \|v_n^l\| - edge^-)^2) \quad (10)$$

where T_i is 1 when class i is present in the data, otherwise is 0. The $edge^+$ and $edge^-$ works as edge which forces the length of the v_n^l into a set of small interval values to minimize the loss. Here the $edge^+$ is set to 0.9 and $edge^-$ is set to 0.1, μ is a regularization parameter, which is set to 0.5 in order to stop the learning and reduce the effect of the negative activity vectors.

D. The activation block

The activation block involves two fully connected layers, which transforms the output activity vectors of the spectral-spatial feature encoder to yield the classification map. The decoder employs the Adam optimizer with a learning rate as follow:

$$L_{end} = L_{margin} + \theta \cdot L_{reconstruction} \quad (11)$$

where θ is set to 0.0005 to balance the weights between L_{margin} and $L_{reconstruction}$ during the reconstruction of loss.

IV. INTERPRETABILITY ASSESSMENT METHODS

We assess the interpretability of the proposed model from three aspects: pre-model, in-model, and post-model interpretability.

A. Pre-model interpretability

In order to evaluate the pre-model interpretability of the proposed pre-processing block, two standard metrics, Shannon entropy and Dunn index, are used to measure and visualize the quality of labelled clusters. Shannon entropy measures the uncertainty and disorder within the information represented by the intermediate features; and the entropy of a class X is defined as:

$$E = - \sum_x p(x) \cdot \log(p(x)) \quad (12)$$

where $p(x)$ is the contribution (or probability) of the feature x to the class X . A low-entropy implies a high-concentration of the feature set within the same class. Dunn index is defined as

the ratio of the minimum inter-class distance and the maximum intra-class distance, thus,

$$D_{index} = \min_{1 \leq i \leq m} \min_{1 \leq j \leq m, i \neq j} \frac{\sigma(C_i, C_j)}{\max_{1 \leq k \leq m} \Delta k} \quad (13)$$

where $\sigma(C_i, C_j)$ is the inter-class distance defined by the L2-norm distance between the class center (mean feature sequence) of class i and j , and $\Delta k = \max_{x, y \in C_i} d(x, y)$ is the intra-class distance defined by the L2-norm distance between any two samples x and y with the same label. A larger Dunn index suggests a better clustering because it indicates a smaller intra-class distance or inter-class distance.

B. In-model interpretability

In our proposed model, the spectral enhanced layers described in Section 3.2 and the capsule layers described in Section 3.3 are the intrinsic interpretable blocks which fully consider the physical mechanism of the spectral combinations and the biological hierarchical interactions among the extracted spectral-spatial features, respectively. In this study, the learning process of the proposed model will be stepwise outputted in order to evaluate the in-model interpretability.

C. Post-model (Post Hoc) interpretability

To evaluate the post model interpretability, auxiliary data are used to explain the biophysical or biochemical meanings of the intermediate features generated in the hidden layers of the model. This is decoupled from the main model, thus, it is only used to evaluate the interpretability of the intermediate layers without affecting the performance of the main model. Therefore, the selection of the auxiliary data is important to explore and have a good understanding of the feature representations in the intermediate layers. In this study, considering the differences in the study cases in landcover classification and crop disease detection, we selected two types of auxiliary data for the post hoc analysis.

1) Vegetation indices data

In order to quantify the biological attributes of the intermediate features extracted in the deep layers, the coefficients of determination (R^2) between such features and biochemical- and biophysical-associated indices are calculated based on univariate correlation analyses. For landcover classification, the ground retrievable parameters represent the biological attributes of the specific vegetation types, we employ 10 popular vegetation indices that have proven to be sensitive to certain biological attributes (see Table I) as substitutes.

2) Biological parameters

For the crop disease monitoring, the measured biological parameters, include leaf area index (LAI), leaf chlorophyll content (CHL), leaf anthocyanin content (ANTH), nitrogen balance index (NBI), and percentile dry matters (PDM). They were synchronously measured at the same place where the HSI measurements were collected. In order to guarantee the sample scale and spatial resolution of HIS data are consistent, a total of 72 sampling sites with $0.05m \times 0.05m$ subplots were set. Wherein, the CHL, ANTH, and NBI were measured by

TABLE I
THE BIOPHYSICAL- AND BIOCHEMICAL-ASSOCIATED VEGETATION INDICES THAT USED IN THIS STUDY

Vegetation index	Relate to	Formula	Ref
Normalized Difference Vegetation Index (NDVI)	Vegetation coverage	$\frac{R_{2600} - R_{550}}{R_{2600} + R_{550}}$	[38]
Photochemical Reflectance Index (PRI)	Photosynthetic efficiency	$\frac{R_{435} - R_{531}}{R_{435} + R_{531}}$	[39]
Red-edge Chlorophyll Index (CRed-edge)	Chlorophyll content	$\frac{R_{680}}{R_{750}} - 1$	[40]
Normalized Difference Water Index (NDWI)	Water	$\frac{R_{1640} - R_{2130}}{R_{1640} + R_{2130}}$	[41]
Triangular Vegetation Index (TVI)	Green LAI	$0.5[120(R_{750} - R_{550}) - 200(R_{670} - R_{550})]$	[42]
Structural Independent Pigment Index (SIPI)	Pigment content	$\frac{R_{680} - R_{445}}{R_{680} + R_{800}}$	[43]
Plant Senescence Reflectance Index (PSRI)	Nutrient	$\frac{R_{678} - R_{550}}{R_{750}}$	[44]
Normalized Pigment Chlorophyll ratio index (NPCCI)	Chlorophyll density	$\frac{R_{680} - R_{430}}{R_{680} + R_{430}}$	[45]
Optimized Soil Adjusted Vegetation Index (OSAVI)	soil background	$\frac{R_{2500} - R_{550}}{R_{2500} + R_{550} + 0.16}$	[46]

the Dualex Scientific sensor (FORCE-A, Inc. Orsay, France), a hand-held leaf-clip sensor designed to non-destructively evaluate the content of pigments and epidermal flavonol. For the LAI acquisition, the LAI-2200 Plant canopy analyzer (Li-Cor Biosciences Inc., Lincoln, NE, USA) was used. For the PDM measurement, 10-12 leaves for each sampling subplot were weighed with an electronic balance (Haozhuang, Inc, Shanghai, China) and dried in an electric blowing drying oven (DGG-9240A, Senxin, Inc, Shanghai, China) over 10 hours. After drying, the percentile dry matter (PDM) of the leaves was calculated by the ratio of dry and fresh weight.

In order to find the linear correlation between the enhanced spectral features after training and the parameters, a correlation analysis is used. The coefficient of determination (R^2) is used to assess the interpretability of such features on the learning process.

V. EXPERIMENTAL EVALUATION

To evaluate the effectiveness of the proposed model, we have applied it to two real datasets (see Table II) and have compared it with six state-of-the-art machine learning models for HIS -based classification tasks: crop type classification and crop disease diagnosis. These six machine learning models include 1) two traditional machine learning approaches, support vector machine (SVM) [47], random forest (RF) [48]; 2) two-dimensional convolutional neural network (2D-CNN) [49]; and 3) three spectral-spatial based deep learning approaches including three-dimensional convolutional neural network (3D-CNN) [50], spectral-spatial residual network (SSRN) [51] and the capsule network (CapNet) [22]. The detailed information and the experimental configurations and evaluation are described below.

A. HSI data description

The two datasets used for the evaluation and validation of the proposed model in this study, include a public available dataset, Indian Pines (IP), and an experimentally measured Wheat Yellow Rust (WYR) dataset. The IP dataset is used for the task of crop type classification, and the WYR data is used for the task of crop diseases diagnosis. The detailed description of these two datasets is presented as follows:

TABLE II
NUMBER OF AVAILABLE SAMPLES IN THE IP AND WYR DATASETS.

IP dataset		WYR dataset	
Land cover type	Samples	Crop status	Samples
Alfalfa	46	Health	10842
Corn-notill	1428	Yellow rust	7682
Corn-min	930	Others	3613
Corn	237		
Grass/Pasture	483		
Grass/Trees	730		
Grass/Pasture-mowed	28		
Hay-windrowed	478		
Oats	20		
Soybeans-notill	972		
Soybeans-min	2455		
Soybeans-clean	593		
Wheat	205		
Woods	1265		
Bldg-Grass-Tree-Drives	386		
Stone-steel towers	93		
Background	10776		

1) IP dataset

IP dataset was collected by the Airborne Visible and Infrared Imaging Spectrometer (AVIRIS) sensor in 1992, which covers the different crop planting areas in north-western Indiana, USA, and contains a total of 16 ground truth classes. This dataset involves 224 hyperspectral bands in the range of 400-2500nm with a size of 145 × 145. The detailed information about the IP data set can be found in [52].

2) WYR dataset

The WYR dataset was collected by the DJI S1000 UAV system (SZ DJI Technology Co Ltd., Gungdong, China) based on UHD-185 Imaging spectrometer (Cubert GmbH, Ulm, Baden-Wrttemberg, Germany) in 2018. This dataset involves the 125 bands from visible to near-infrared bands between 450 and 950nm with a size of 16279 × 14762. All the images were obtained at a flight height of 30 m, with a spatial resolution close to 2cm per pixel. Hyperspectral images were manually labelled based on the ground synchronization survey of the occurrence conditions of yellow rust.

B. Evaluation metrics

To valid the effectiveness of the proposed model, we have used the following metrics: the overall accuracy and recalled accuracy [53], sensitivity and specificity [54], kappa coefficient [55] and execution time.

C. Model evaluation and interpretability analysis

1) *Case Study 1: the ground surface classification using Indian Pines (IP) dataset:* The first experiment is used to evaluate the performance of the proposed network on the classification of crop types using the IP dataset. Table III provides a quantitative accuracy assessment and classification comparison of the proposed approach, together with the six approaches, SVM, RF, 2D CNN, 3D CNN, SSRN, and CapNet. In all of the tests and comparisons, two-thirds of the labelled pixels were randomly selected as the training dataset, and the remaining pixels were used as the testing dataset. Comparing to the existing methods, the proposed model shows a significant improvement in the classification performance.

TABLE III
ACCURACY EVALUATION FOR THE CLASSIFICATION OF IP DATASET.

Class	Proposed	SVM	RF	2D-CNN	3D-CNN	SSRN	CapNet
Alfalfa	98.2	81.5	62.5	80.1	75.2	98.1	95.4
Corn-notill	98.4	76.1	56.2	75.2	92.2	95.2	95.8
Corn-min	98.7	71.4	41.2	82.1	88.1	96.7	96
Corn	97.2	94.2	82.5	69.2	84.5	93.6	96.1
Grass/Pasture	98.8	93.3	92.1	88.3	86.5	95	98.3
Grass/Pasture-mowed	96.6	84.2	31.5	67.2	72.5	92.9	94.2
Grass/Trees	99.1	91.3	88.4	92.8	89.2	94.4	98.4
Hay-windrowed	99.5	51.4	13.9	67	56.5	96.2	99.4
Oats	98.1	75	55.9	68.2	97.2	96.2	97.4
Soybeans-notill	97.4	83.5	88.2	66.1	98.1	96.2	95.3
Soybeans-min	97.7	84.6	55.4	81.2	93.5	95.5	96.8
Soybeans-clean	96.4	94.2	91.2	72.1	99.6	93.8	93.6
Wheat	99.1	96.1	97.4	91.2	92.4	94.5	97.4
Woods	97.2	67.4	49.2	92.3	96.2	95.2	95.5
Bldg-Grass-Tree-Drives	97.6	81.2	88.4	82.2	90.3	93.2	96.5
Stone-steel towers	96.2	82.2	82.3	93.3	92.1	95.3	95.4
Background	94.6	67.2	33.4	65.7	88.1	90.3	92.4
Avg. sensitivity (%)	98.55	81.98	66.23	79.42	88.71	94.84	96.11
Avg. specificity (%)	97.69	81.47	65.86	79.18	88.47	94.32	95.54
OA(%)	98.65	81.7	67.57	78.66	89.5	96.3	97.59
AA(%)	97.69	80.87	65.27	78.48	87.76	94.84	96.11
Kappa	0.85	0.69	0.5	0.78	0.82	0.83	0.81
Time (s)	305.2	44.8	65.2	110.5	117.4	245.3	217.5

For example, the overall and average accuracies of the proposed approach respectively reaches 98.7% and 97.7%, with a Kappa value of 0.85; the average sensitivity and specificity are 98.55% and 97.69% respectively. Among the competitors, the CapNet achieves the second best classification performance (OA=97.6%, AA=96.1%, Kappa=0.81, the average sensitivity of 96.11%, and average specificity of 95.53%). Following the CapNet, the SSRN achieves an overall and average accuracy of 96.3% and 94.8%, a Kappa of 0.83, average sensitivity of 94.81%, and average specificity of 94.32%. The lowest classification accuracy is occurred for the hay-windrowed, it only achieves an accuracy of 51.4% and 13.9% by the machine learning-based SVM and RF classifiers, respectively. In comparison, the deep learning-based classifiers are able to achieve an improved classification, wherein, the proposed approach obtains the highest accuracy of 99.5%. Just like our proposed method, the CapNet and SSRN also exploit joint spectral-spatial information and provide better classification performance than the traditional machine learning models using single type of features (either spectral or spatial information). Overall, the proposed approach outperforms the CapNet and SSRN with a considerable improvement in the evaluation of indices in terms of average sensitivity, average specificity, OA, AA, and Kappa. Regarding the computing time, because of the two-stage feature learning architecture of the proposed model, it requires more computing resources and time, and the average computing time reaches 305.2s for the multi-classifications task, which is the slowest among all of the competitors.

Fig. 4 illustrates the detailed comparison of the sensitivity and specificity of each vegetation categories in the IP dataset. It shows that the sensitivity and specificity of the deep learning based classifiers are higher than those of two traditional machine learning based classifiers, SVM and RF. Besides, among all of the 17 vegetation categories, the proposed approach achieves the highest sensitivity and specificity in 16 classes (except the soybeans-clean), which indicates that the

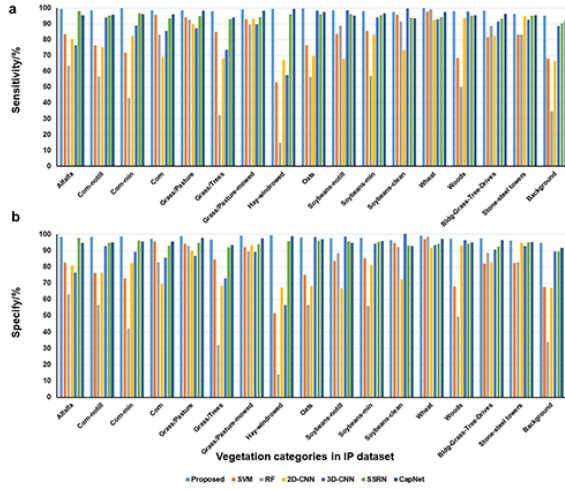


Fig. 4. Multi-class comparison between the different vegetation categories in IP dataset. (a) the sensitivity of the proposed approach and the competitors for each vegetation class. (b) the specificity of the proposed approach and the competitors for each vegetation class

performance of the proposed approach outperforms the other competitors in the leakage and misclassification.

Fig. 5 demonstrates the classification maps which is corresponding to the accuracy evaluation in Table 3. Because only the spectral signature of each pixel is considered in the traditional machine learning models, there are noticeable salt and paper noises found in the classification maps produced by SVM and RF (Fig. 5c and 5d). On the other hand, as a typical neural network model, the 2D CNN generally introduces some misclassification in class boundaries (Fig. 5e). The main reason is due to the typical defect of the 2D CNN, where only spatial information is involved in the convolution process of the model, which makes the classification more sensitive to spatial scales of the pre-defined window size. The spectral-spatial classifiers (i.e. 3D CNN, SSRN, CapNet, and the proposed approach) demonstrates a higher performance in the accuracy and class consistency of ground surface classification than SVM, RF and 2D-CNN where only the spectral or spatial signal is considered. Although the similar classification maps are illustrated in Fig. 5f-i, the map produced by our proposed approach shows fewer misclassified pixels and clearer class edge and delineation than the results of 3DCNN, SSRN, and CapNet. In addition, if we compare the labelled and unlabelled (not covered in Fig. 5b) areas, there are less potential outliers in the resultant map of the proposed model. This indicates that the proposed model provides more consistent results in the task of ground surface classification than other five methods.

2) *Case Study 2: the crop stress detection using the WYR dataset:* The second experiment is used to evaluate the performance of the proposed method on crop disease detection using the WYR dataset.

Considering SVM, RF, and 2D CNN can only handle one type of information (spectral or spatial), only the spectral-spatial classifiers (i.e. 3D CNN, SSRN, and CapNet) were compared against the proposed approach. In this study, 70% labelled data are randomly selected as the training samples and

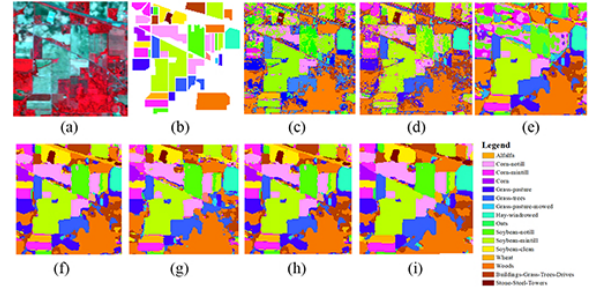


Fig. 5. The comparison of the classification maps of Indian Pine dataset. (a) the false colour composition map of the raw data. (b) Ground-truth data used in the training and evaluation of the models. (c-i) the classification result of SVM, RF, 2D-CNN, 3D-CNN, SSRN, CapNet, and the proposed model, respectively.

the rest 30% are used as the testing samples. Table IV shows the overall accuracy (OA) of 3DCNN, SSRN, CapNet, and the proposed approach using five different window sizes, 9×9 , 15×15 , 21×21 , 27×27 , and 33×33 . The results demonstrate that the proposed approach consistently outperforms the other three models in most cases of the parameter configuration (except for the window size of 33×33). More specifically, the proposed approach provides an OA improvement up to 13.41% for 9×9 kernel, 6.63% for 15×15 kernel, 10.41% for 21×21 kernel, and 10.57% for 27×27 kernel, respectively. For the window size of 33×33 , the OA of the proposed approach is slightly lower (0.01) than that of CapNet. One explanation for this exception may lie in the fact that the proposed model is sequentially learning the heterogeneities in spectral and spatial dimensions. The input patch with a 33×33 window size would beyond the width of the wheat leaf under the spatial resolution of 0.02m, and it may involve mixed patterns in the neurons of the learning process.

In addition, Table V provides a detailed comparison of the confusion matrix of 3DCNN, SSRN, CapNet, and the proposed approach. Firstly, when the input patch in the range from 9×9 to 27×27 , a larger window size generally leads to a higher classification accuracy. One possible explanation is that the larger the input size is, the more spectral-spatial pattern information is learned by the models. Secondly, the proposed approach requires a smaller window size to achieve a similar classification performance, or achieve a higher accuracy with the same configuration of window size when compared with the competitors. For instance, the average accuracy of the proposed approach with a window size of 9×9 reaches 90.19%, 2.38% higher than the second accuracy (i.e. 87.81%) produced by the CapNet with the same window size. It is similar to the accuracy value of 89.9% achieved by the CapNet with the window size of 27×27 . The possible reason is that the featured tensor composed by the capsule units reinforces the generalization capability of the spectral-spatial information in characterizing the target items, and represents the heterogeneity and rotation invariance of each labelled class. Such findings suggest that the proposed model is not only able to describe more interpretable features in the learning process, but also able to increase the efficiency and accuracy of the classification.

TABLE IV
THE OVERALL ACCURACY (OA, %) OF THE 3DCNN, SSRN, CAPNET,
AND PROPOSED APPROACH USING DIFFERENT WINDOW SIZE OF INPUT
PATCH FOR CROP STRESS DETECTION BASED ON WYR DATASET

Spatial size	3DCNN	SSRN	CapNet	Proposed
9×9	76.72	83.66	87.72	90.13
15×15	81.12	84.01	88.11	90.75
21×21	80.41	85.01	88.08	90.82
27×27	80.44	84.49	88.49	91.01
33×33	81.01	84.56	90.5	90.49

TABLE V
THE DETAILED PERFORMANCE COMPARISON OF THE 3DCNN, SSRN,
CAPNET, AND PROPOSED APPROACH USING DIFFERENT WINDOW SIZE OF
INPUT PATCH FOR CROP STRESS DETECTION BASED ON WYR DATASET.

Class	3DCNN				
	9×9	15×15	21×21	27×27	33×33
healthy wheat(%)	79.52	81.41	80.64	80.66	81.53
Yellow rust(%)	76.31	78.74	78.31	78.58	78.31
Soil(%)	83.61	83.7	83.78	83.82	83.4
Avg. sensitivity (%)	91.16	92.2	93	92.35	91.42
Avg. specificity(%)	93	92.58	93.05	93.39	93.31
AA (%)	79.81	81.28	80.91	81.02	81.08
Kappa	0.78	0.8	0.8	0.81	0.8

Class	SSRN				
	9×9	15×15	21×21	27×27	33×33
healthy wheat(%)	83.63	84.65	85.93	84.04	84.8
Yellow rust(%)	80.67	81.95	82.74	81.94	81.41
Soil(%)	86.08	86.14	86.42	86.87	86.64
Avg. sensitivity (%)	81.1	83.66	82.37	82.56	82.12
Avg. specificity(%)	83.2	83.8	83.42	83.43	83.3
AA (%)	83.46	84.25	85.03	84.28	84.28
Kappa	0.82	0.83	0.83	0.84	0.84

Class	CapNet				
	9×9	15×15	21×21	27×27	33×33
healthy wheat(%)	88.06	88.93	88.97	91.08	91.91
Yellow rust(%)	86.11	86.45	86.96	87.39	87.44
Soil(%)	89.26	89.23	89.48	91.24	92.7
Avg. sensitivity (%)	84.5	85.73	87.28	85.85	85.3
Avg. specificity(%)	85.27	85.95	87.13	86.34	86.67
AA (%)	87.81	88.2	88.47	89.9	90.68
Kappa	0.85	0.85	0.86	0.86	0.87

Class	Proposed				
	9×9	15×15	21×21	27×27	33×33
healthy wheat(%)	90.11	90.96	90.89	91.42	91.16
Yellow rust(%)	88.6	88.61	89.45	89.68	88.8
Soil(%)	91.87	91.77	91.77	91.97	91.64
Avg. sensitivity (%)	89	90.1	89.39	90.72	92.44
Avg. specificity(%)	9.44	90.44	30.68	92.56	93.7
AA (%)	90.19	90.45	90.7	91.02	90.53
Kappa	0.88	0.89	0.91	0.94	0.92

Fig. 6 illustrates the detailed comparison of the sensitivity and specificity between the proposed approach and its competitors with various window sizes for each class in the WYR dataset. Similar to the accuracy assessment results, the proposed approach achieves better sensitivity and specificity with the window size from 9×9 to 27×27 than the other models, and the highest values occurs in the window size of 21×21 . This suggests that the proposed approach may achieve the best classification for the WYR dataset with the window size of 21×21 . For the purpose of demonstration, Fig. 7 shows the classification maps of wheat yellow rust from a winter wheat field plot produced by the 3DCNN, SSRN, CapNet, and the proposed approach with a window size of 27×27 . The comparison of these four maps illustrates that the proposed approach outperforms the competitors in the class delineation

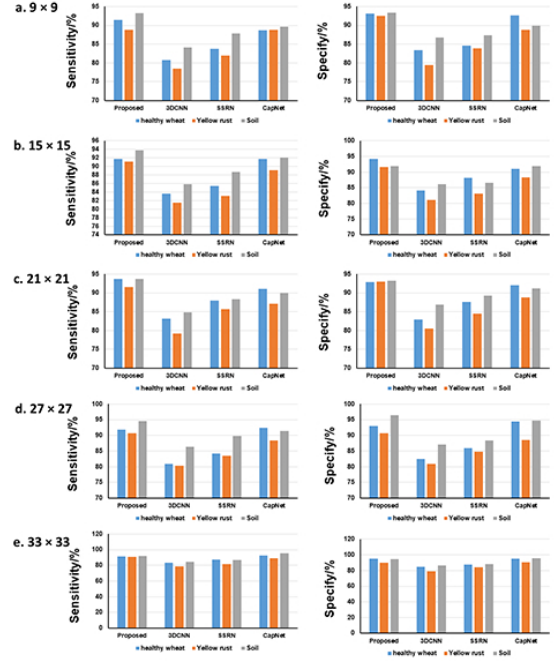


Fig. 6. The comparison of the sensitivity and specificity of the proposed approach and the spectral–spatial classifier with the window size from 9×9 to 33×33 (a – e)

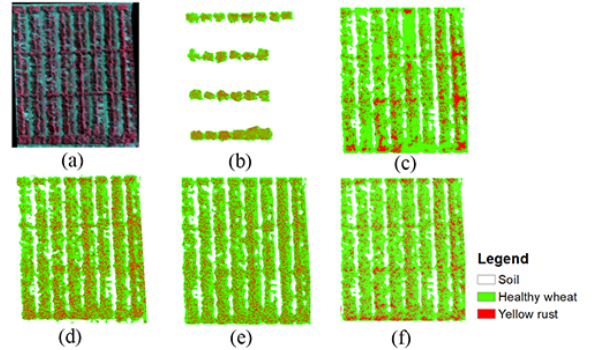


Fig. 7. The comparison of the classification maps of wheat yellow rust dataset. (a) the false colour composition map of the raw data. (b) Ground-truth data used in the training and evaluation of the models. (c – f) the classification result of 3D-CNN, SSRN, CapNet, and the proposed model, respectively

and distribution of yellow rust. Specifically, the class boundaries of yellow rust pixels obtained by the proposed approach are clearer and more precise, such boundary characterization is identical with the typical yellow rust pathogen features observed at the canopy scale. In addition, the yellow rust class contains stripe features, which have been better delineated in the maps obtained from the proposed approach. Moreover, by comparing with the classification results over unlabelled areas, there is a noticeable consistency in classification with better pathological distribution features, which also suggests that the proposed approach provides a better generalization performance on the detection of wheat yellow rust than its competitors.

Fig. 8 shows the variations of the convergence of the proposed network architecture and its competitors with a

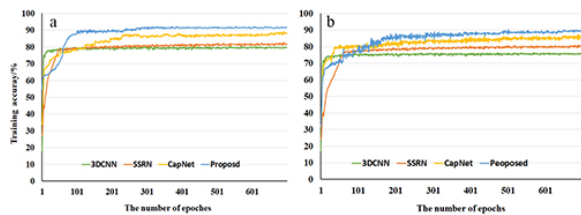


Fig. 8. Evolution of the (a) training and (b) testing accuracy (in %) of 3DCNN, SSRN, CapNet, and the proposed approach with a window size of 27×27 based on the WYR data set

window size of 27×27 and an epoch number of 700. The results demonstrate that the proposed approach provides a stable accuracy in both training and testing processes (i.e. the average accuracies reached 91.2% and 89.9%, respectively). Meanwhile, the accuracy results show the tendency of decline for other algorithms (3DCNN, SSRN, and CapNet) during the training and testing processes. For instance, the average training accuracy of the 3DCNN reached 79.9%, but its testing accuracy only reaches 75.2%. The possible reason for such accuracy decline phenomenon is due to the black-box learning process in the intermediate layers, which always lead the traditional network architecture to a local optimum. This occurs when the scale of sampling is not big enough to cover all of the possible states of the target classes. In this case, benefiting from the physical mechanism and interpretability discussed in previous sections, the learning process of the proposed method is able to represent the biophysical and biochemical variations and the spatial structure characteristics between the healthy wheat and the wheat infected with yellow rust. This explains why the proposed approach provides a greater performance in classification accuracy and robustness than the other models.

Regarding the convergence, it is noteworthy that the training accuracy of the proposed approach (the blue line in Fig. 8a) reveals an S-shape curve, and we can separate this progress into four parts. At the beginning, the rate of convergence is slow during the first 50^{th} epochs. And then, this rate increases dramatically from 51^{th} to 120^{th} epochs. After this point, the training accuracy reveals a fluctuation between the 88.2% and 90.5% from the 121^{th} to 330^{th} epochs. Finally, the accuracy is stabilized at around 91.02%. This tendency may associate with the two-stage network architecture of the proposed model, the training and extraction of sensitive spectral features in the first stage would produce a chain reaction for the learning process of the second stage and the final accuracy. Similarly, although the convergence rate of the proposed approach in the testing process is faster than that in the training process, it is still slower than the other three methods.

D. Interpretability analysis

The interpretability of the model is one of the most important contributions in our work. We evaluate it from three perspectives: 1) pre-model interpretability, 2) post hoc analysis, 3) in-model interpretability with the methods introduced in Section 4.2

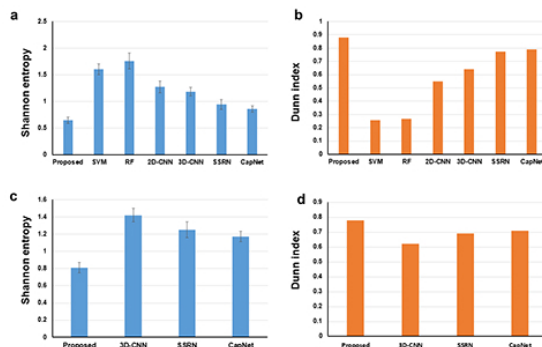


Fig. 9. Shannon entropy and Dunn index for IP datasets (a-b) and WYR datasets (c-d). The values entropy is calculated for each class, then averaged all of them. The error bars represent the standard deviation across the classes

1) *Pre-model interpretability*: The Shannon entropy and Dunn index are used to evaluate the effect of the spectral segmentation layer on uncertainty and cluster of the features in the main model (see Fig. 9). The Shannon entropy of each class is calculated by averaging all feature vectors within it, and the entropy values presented in Fig. 9 is the average of all classes.

Fig. 9 indicates that, in comparison with its competitors, our proposed approach achieves a lower Shannon entropy (i.e. intra-class disorder) and a higher Dunn index (i.e. inter-class clustering) in both vegetation classification (Fig. 9a-b) and crop disease detection (Fig. 9c-d). The rationale behind is that the spectral segmentation layer provides a physical constraint on the raw HSI data, which makes the learning process of the main model conduct in the band ranges with explicit spectral-biological attributes. Therefore, the intermediate features produced by the proposed approach may provide greater representations of the intrinsic inter-class differences and lower statistical-derived learning error than the other models.

E. Post-model (post hoc) analysis

In this work, the post hoc analysis mainly focuses on the first learning stage of the proposed network, the aim of the post hoc analysis is to explore the biological correlation of the spectral features produced by the spectral enhancement layers with the auxiliary ground datasets. For Case Study 1, Fig. 10a shows the correlation relationship between the spectral segmentation-based features produced by the spectral enhancement layers of Stage 1 and the pre-selected vegetation indices, which reveals the potential spectral-derived biological properties of the enhanced spectral features. For instance, the red-edge and near-infrared associated features reveal the highest coefficient of determination (R^2) with the canopy structure associated SVIs, such as NDVI, PRI, and CIred-edge. Such correlations not only indicate the statistical representations of the generated spectral features, but also represent the subtle reflectance differences between the different plant categories in the Indian Pines dataset. Similarly, Fig. 10b shows the correlation graph between the enhanced spectral features and the ground measured auxiliary parameters for

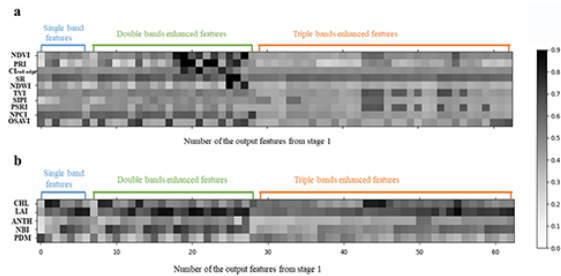


Fig. 10. The visualization of the correlation of the between the ground measured parameters and the extracted features from spectral enhance layers for (a) IP dataset and (b) WYR dataset

the WYR dataset based disease detection task, which reveals the potential biophysical and biochemical properties hidden in the enhanced spectral features. For instance, the red and red-edge associated features reveals the highest coefficient of determination (R^2) with the ground measured LAI, the green and red associated features exhibit a higher sensitivity with ground measured CHL. These findings from the two case studies based on the IP and WRY datasets has proven that the intermediate features can characterise not only the statistical properties for the corresponding classes, but also their biophysical and biochemical attributes, which provides the interpretability of the biological differences between the target classes.

E. In-model interpretability

The main model split the learning process into two stages: the spectral significance enhancement and spectral-spatial hierarchical construction. These two stages sequentially explore the spectral significance by extracting the biological associated spectral signature from the HSI data, and represent spectral-spatial hierarchical structure of the target class by encapsulating the extracted spectral-spatial information into capsule features. Besides, such a two-stage learning architecture would improve the observation and explanation of the evolution of the features in different layers. Because the biological interpretability of the outputs in Stage 1 (i.e. the enhanced spectral feature sets) has been proven in Section 5.4.2, here, we only discuss whether the biological interpretability at the high-level capsule features can be achieved by the intrinsic architecture of the model. Specifically, Fig. 11 illustrates the visualization of the weights of the 3×3 convolutional kernels in *conv3* layer, the outputted feature maps and feature capsules from the capsule layers for both IP and WYR datasets.

For Case study 1, Fig. 11a visualises the 3×3 weights of the *conv3* layer, which provides a direct way to understand the evolution progress of the intermediate features. It is noteworthy that the weights of the 3×3 convolutional kernels after training red, red-edge, and near-infrared associated features are higher than other features, which means the spectral features from red, red-edge, and near-infrared segmentations are more sensitive to the HSI texture signatures (i.e the canopy structure characteristics in the IP dataset). This finding is also in agreement with previous studies [45], [56]. The final feature maps and the capsulized feature vectors from the

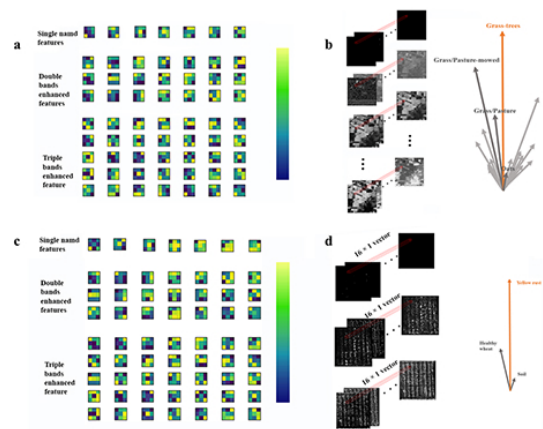


Fig. 11. The visualization of the weights of the 3×3 convolutional kernels in *conv3* layer and the outputted feature maps and feature capsules of the capsule layers for Case Study 1: vegetation classification of IP datasets, (a-b) and Case Study 2: disease detection of WYR dataset, (c-d).

capsule layers are shown in Fig. 11b. where the well-designed capsule layer is able to manage the intermediate scalar features throughout the network, and also calculate the corresponding instantiation parameters to represent the hierarchical structure and potential transformations of the target classes. This will help better characterising the rotation invariance of spectral and spatial features of each class. The length of each feature vector are used to estimate the probability that a specific spectral-spatial feature occurred in each of the class, and final classification would be determined by the maximum length.

For Case Study 2, the visualization of 3×3 weights of the *conv3* layer (see Fig. 11c) also provides a direct way to understand the contribution of each intermediate feature in the spatial-dimension. It is noteworthy that, in a 3×3 convolution kernel, the weights of the neighbour pixels for the features sensitive to the biophysical parameters (e.g. LAI, PDM) are generally higher than the features sensitive to biochemical parameters (e.g. CHL, ANTH). This indicates that, comparing with the biochemical parameters, the texture information and spatial pattern provide more representations of the physical parameters in the detection and classification of yellow rust. In other words, the proposed approach provides better capability in characterizing the appearance symptom (e.g. leaf rolling, wither) when the wheat is infected by yellow rust. The feature maps from the class-capsules layer are shown in Fig. 11d, the spectral-spatial features are integrated into three feature vectors, the length of each are used to estimate the probability that a specific biophysical and biochemical feature occurred in each of the class, and final classification would be determined by the maximum length.

VI. CONCLUSION

In this study, a new deep learning architecture based on two-stage spectral-spatial feature learning is presented to achieve an effective classification with a biological interpretable learning from HIS data. Specifically, the proposed network firstly split the input HSI data into 7 spectral segmentations, where the most valuable spectral features sensitive to the reflectance

and radiation properties of the target classes are extracted by the 1D-CNN based layers. Subsequently, a set of enhanced features with the explicit biophysical and biochemical properties are generated by a well-designed feature enhancement layer to characterize the biological associated properties of each class. Finally, a series of spectral-spatial capsule units are employed to output the feature vectors that represent the enhanced feature set as a collection of canonical spectral-spatial pattern and the specific individual instantiation parameters at a higher level. Through this network, the intermediate features uncover more biological and structural patterns of the target ground objectives, which subsequently leads to an increasing interpretability and a reduction of the computing complexity, and therefore, a more accurate model convergence. The comparison with the state-of-the-art models for HSI data classification, reveals that the proposed BIT-DNN exhibits a competitive performance in classification accuracy.

The most important contribution of the proposed approach lies in its interpretable learning process. It can uncover the potential biological and structural patterns of the target items from the inherent spectral-spatial complexity of the HSI data, and the potential transformation and rotation by means of a neural hierarchy structure, which disentangles such biological and structural associated features from the instantiation parameters. Therefore, the high-level feature capsules would be activated by the prediction agreement of the lower-level features, and it intrinsically builds the connections to better express the rotational invariance of the combination of the biological and structure features, and further achieves consistently high classification accuracy on both the tasks of plant categories classification and crop disease detection.

ACKNOWLEDGMENT

This research is supported by BBSRC (BB/R019983/1), BBSRC (BB/S020969/1). The work is also supported by Newton Fund Institutional Links grant, ID 332438911, under the Newton-Ungku Omar Fund partnership (the grant is funded by the UK Department of Business, Energy, and Industrial Strategy (BEIS) and the Malaysian Industry-Government Group for High Technology and delivered by the British Council. For further information, please visit www.newtonfund.ac.uk.)

REFERENCES

- [1] A. Kamilaris and F. X. Prenafeta-Bold, "Deep learning in agriculture: A survey," *Computers and electronics in agriculture*, vol. 147, pp. 70–90, 2018.
- [2] Y.-Y. Zheng, J.-L. Kong, X.-B. Jin, X.-Y. Wang, T.-L. Su, and M. Zuo, "Cropdeep: the crop vision dataset for deep-learning-based classification and detection in precision agriculture," *Sensors*, vol. 19, no. 5, p. 1058, 2019.
- [3] N. Jordan, R. Becker, J. Gunsolus, S. White, and S. Damme, "Knowledge networks: an avenue to ecological management of invasive weeds," *Weed Science*, vol. 51, no. 2, pp. 271–277, 2003.
- [4] J. Ma and H. Yuan, "Bilstm+ crfbased named entity recognition in scientific papers in the field of ecological restoration technology," *Proceedings of the Association for Information Science and Technology*, vol. 56, no. 1, pp. 186–195, 2019.
- [5] H. Lee, R. Grosse, R. Ranganath, and A. Y. Ng, "Convolutional deep belief networks for scalable unsupervised learning of hierarchical representations," in *Proceedings of the 26th annual international conference on machine learning*. ACM, Conference Proceedings, pp. 609–616.
- [6] Y. Xu, T. Mo, Q. Feng, P. Zhong, M. Lai, I. Eric, and C. Chang, "Deep learning of feature representation with multiple instance learning for medical image analysis," in *2014 IEEE international conference on acoustics, speech and signal processing (ICASSP)*. IEEE, Conference Proceedings, pp. 1626–1630.
- [7] A. Bettge, R. Roscher, and S. Wenzel, "Deep self-taught learning for remote sensing image classification," *arXiv preprint arXiv:1710.07096*, 2017.
- [8] D. Lin, "Deep unsupervised representation learning for remote sensing images," *arXiv preprint arXiv:1612.08879*, 2016.
- [9] M. Reichstein, G. Camps-Valls, B. Stevens, M. Jung, J. Denzler, and N. Carvalhais, "Deep learning and process understanding for data-driven earth system science," *Nature*, vol. 566, no. 7743, pp. 195–204, 2019.
- [10] X. X. Zhu, D. Tuia, L. Mou, G.-S. Xia, L. Zhang, F. Xu, and F. Fraundorfer, "Deep learning in remote sensing: A comprehensive review and list of resources," *IEEE Geoscience and Remote Sensing Magazine*, vol. 5, no. 4, pp. 8–36, 2017.
- [11] F. Hu, G.-S. Xia, J. Hu, and L. Zhang, "Transferring deep convolutional neural networks for the scene classification of high-resolution remote sensing imagery," *Remote Sensing*, vol. 7, no. 11, pp. 14680–14707, 2015.
- [12] L. Mou, P. Ghamisi, and X. X. Zhu, "Fully conv-deconv network for unsupervised spectral-spatial feature extraction of hyperspectral imagery via residual learning," in *2017 IEEE International Geoscience and Remote Sensing Symposium (IGARSS)*. IEEE, Conference Proceedings, pp. 5181–5184.
- [13] J. S. Yi, Y. ah Kang, and J. Stasko, "Toward a deeper understanding of the role of interaction in information visualization," *IEEE transactions on visualization and computer graphics*, vol. 13, no. 6, pp. 1224–1231, 2007.
- [14] S. Cai, Q. Du, and R. J. Moorhead, "Feature-driven multilayer visualization for remotely sensed hyperspectral imagery," *IEEE Transactions on Geoscience and Remote Sensing*, vol. 48, no. 9, pp. 3471–3481, 2010.
- [15] A. E. Maxwell, T. A. Warner, and F. Fang, "Implementation of machine-learning classification in remote sensing: An applied review," *International Journal of Remote Sensing*, vol. 39, no. 9, pp. 2784–2817, 2018.
- [16] D. Lin, K. Fu, Y. Wang, G. Xu, and X. Sun, "Marta gans: Unsupervised representation learning for remote sensing image classification," *IEEE Geoscience and Remote Sensing Letters*, vol. 14, no. 11, pp. 2092–2096, 2017.
- [17] J. Zhu, L. Wu, H. Hao, X. Song, and Y. Lu, "Auto-encoder based for high spectral dimensional data classification and visualization," in *2017 IEEE Second International Conference on Data Science in Cyberspace (DSC)*. IEEE, Conference Proceedings, pp. 350–354.
- [18] Z. Wang, L. Tang, X. Liu, Z. Yao, S. Yi, J. Shao, J. Yan, S. Wang, H. Li, and X. Wang, "Orientation invariant feature embedding and spatial temporal regularization for vehicle re-identification," in *Proceedings of the IEEE International Conference on Computer Vision*, Conference Proceedings, pp. 379–387.
- [19] C. Molnar, *Interpretable machine learning*. Lulu.com, 2019.
- [20] Y. Gao, X. Wang, Y. Cheng, and Z. J. Wang, "Dimensionality reduction for hyperspectral data based on class-aware tensor neighborhood graph and patch alignment," *IEEE transactions on neural networks and learning systems*, vol. 26, no. 8, pp. 1582–1593, 2014.
- [21] M. T. Ribeiro, S. Singh, and C. Guestrin, "Model-agnostic interpretability of machine learning," *arXiv preprint arXiv:1606.05386*, 2016.
- [22] M. E. Paoletti, J. M. Haut, R. Fernandez-Beltran, J. Plaza, A. Plaza, J. Li, and F. Pla, "Capsule networks for hyperspectral image classification," *IEEE Transactions on Geoscience and Remote Sensing*, vol. 57, no. 4, pp. 2145–2160, 2018.
- [23] D. Goswami, "Application of capsule networks for image classification on complex datasets," Thesis, 2019.
- [24] V. Nagarajan and J. Z. Kolter, "Gradient descent gan optimization is locally stable," in *Advances in Neural Information Processing Systems*, Conference Proceedings, pp. 5585–5595.
- [25] D. Crever and R. Lepage, "Knowledge-based image understanding systems: A survey," *Computer vision and image understanding*, vol. 67, no. 2, pp. 161–185, 1997.
- [26] G. Forestier, A. Puissant, C. Wemmert, and P. Ganarski, "Knowledge-based region labeling for remote sensing image interpretation," *Computers, Environment and Urban Systems*, vol. 36, no. 5, pp. 470–480, 2012.
- [27] X. Li, X. Cheng, W. Chen, G. Chen, and S. Liu, "Identification of forested landslides using lidar data, object-based image analysis, and machine learning algorithms," *Remote sensing*, vol. 7, no. 8, pp. 9705–9726, 2015.

- [28] W. Zhao and S. Du, "Spectralspatial feature extraction for hyperspectral image classification: A dimension reduction and deep learning approach," *IEEE Transactions on Geoscience and Remote Sensing*, vol. 54, no. 8, pp. 4544–4554, 2016.
- [29] J. Yang, Y.-Q. Zhao, and J. C.-W. Chan, "Learning and transferring deep joint spectralspatial features for hyperspectral classification," *IEEE Transactions on Geoscience and Remote Sensing*, vol. 55, no. 8, pp. 4729–4742, 2017.
- [30] J. Choo and S. Liu, "Visual analytics for explainable deep learning," *IEEE computer graphics and applications*, vol. 38, no. 4, pp. 84–92, 2018.
- [31] S. Ghosal, D. Blystone, A. K. Singh, B. Ganapathysubramanian, A. Singh, and S. Sarkar, "An explainable deep machine vision framework for plant stress phenotyping," *Proceedings of the National Academy of Sciences*, vol. 115, no. 18, pp. 4613–4618, 2018.
- [32] K. Makantasis, K. Karantzalos, A. Doulamis, and N. Doulamis, "Deep supervised learning for hyperspectral data classification through convolutional neural networks," in *2015 IEEE International Geoscience and Remote Sensing Symposium (IGARSS)*. IEEE, Conference Proceedings, pp. 4959–4962.
- [33] J. Yue, W. Zhao, S. Mao, and H. Liu, "Spectralspatial classification of hyperspectral images using deep convolutional neural networks," *Remote Sensing Letters*, vol. 6, no. 6, pp. 468–477, 2015.
- [34] Y. Guo, Y. Liu, A. Oerlemans, S. Lao, S. Wu, and M. S. Lew, "Deep learning for visual understanding: A review," *Neurocomputing*, vol. 187, pp. 27–48, 2016.
- [35] C. ChavanaBryant, Y. Malhi, J. Wu, G. P. Asner, A. Anastasiou, B. J. Enquist, E. G. C. Caravasi, C. E. Doughty, S. R. Saleska, and R. E. Martin, "Leaf aging of amazonian canopy trees as revealed by spectral and physiochemical measurements," *New Phytologist*, vol. 214, no. 3, pp. 1049–1063, 2017.
- [36] E. M. Middleton, K. F. Huemmrich, Y.-B. Cheng, and H. A. Margolis, *12 spectral bioindicators of photosynthetic efficiency and vegetation stress*. CRC Press, 2016, pp. 265–288.
- [37] S. Sabour, N. Frosst, and G. E. Hinton, "Dynamic routing between capsules," in *Advances in neural information processing systems*, Conference Proceedings, pp. 3856–3866.
- [38] J. Cihlar, L. S. Laurent, and J. Dyer, "Relation between the normalized difference vegetation index and ecological variables," *Remote sensing of Environment*, vol. 35, no. 2-3, pp. 279–298, 1991.
- [39] J. Gamon, L. Serrano, and J. Surfus, "The photochemical reflectance index: an optical indicator of photosynthetic radiation use efficiency across species, functional types, and nutrient levels," *Oecologia*, vol. 112, no. 4, pp. 492–501, 1997.
- [40] J. G. Clevers and A. A. Gitelson, "Remote estimation of crop and grass chlorophyll and nitrogen content using red-edge bands on sentinel-2 and-3," *International Journal of Applied Earth Observation and Geoinformation*, vol. 23, pp. 344–351, 2013.
- [41] S. K. McFeeters, "The use of the normalized difference water index (ndwi) in the delineation of open water features," *International journal of remote sensing*, vol. 17, no. 7, pp. 1425–1432, 1996.
- [42] D. Haboudane, J. R. Miller, E. Pattey, P. J. Zarco-Tejada, and I. B. Strachan, "Hyperspectral vegetation indices and novel algorithms for predicting green lai of crop canopies: Modeling and validation in the context of precision agriculture," *Remote sensing of environment*, vol. 90, no. 3, pp. 337–352, 2004.
- [43] J. Penuelas, F. Baret, and I. Filella, "Semi-empirical indices to assess carotenoids/chlorophyll a ratio from leaf spectral reflectance," *Photosynthetica*, vol. 31, no. 2, pp. 221–230, 1995.
- [44] S. Ren, X. Chen, and S. An, "Assessing plant senescence reflectance index-retrieved vegetation phenology and its spatiotemporal response to climate change in the inner mongolian grassland," *International journal of biometeorology*, vol. 61, no. 4, pp. 601–612, 2017.
- [45] I. Filella and J. Penuelas, "The red edge position and shape as indicators of plant chlorophyll content, biomass and hydric status," *International Journal of Remote Sensing*, vol. 15, no. 7, pp. 1459–1470, 1994.
- [46] G. Rondeaux, M. Steven, and F. Baret, "Optimization of soil-adjusted vegetation indices," *Remote sensing of environment*, vol. 55, no. 2, pp. 95–107, 1996.
- [47] D. V. Carvalho, E. M. Pereira, and J. S. Cardoso, "Machine learning interpretability: A survey on methods and metrics," *Electronics*, vol. 8, no. 8, p. 832, 2019.
- [48] M. Pal, "Random forest classifier for remote sensing classification," *International Journal of Remote Sensing*, vol. 26, no. 1, pp. 217–222, 2005.
- [49] Q. Wang, Z. Yuan, Q. Du, and X. Li, "Getnet: A general end-to-end 2-d cnn framework for hyperspectral image change detection," *IEEE Transactions on Geoscience and Remote Sensing*, vol. 57, no. 1, pp. 3–13, 2018.
- [50] S. Hussein, K. Cao, Q. Song, and U. Bagci, "Risk stratification of lung nodules using 3d cnn-based multi-task learning," in *International conference on information processing in medical imaging*. Springer, Conference Proceedings, pp. 249–260.
- [51] Z. Zhong, J. Li, Z. Luo, and M. Chapman, "Spectralspatial residual network for hyperspectral image classification: A 3-d deep learning framework," *IEEE Transactions on Geoscience and Remote Sensing*, vol. 56, no. 2, pp. 847–858, 2017.
- [52] R. O. Green, M. L. Eastwood, C. M. Sarture, T. G. Chrien, M. Aronsson, B. J. Chippendale, J. A. Faust, B. E. Pavri, C. J. Chovit, and M. Solis, "Imaging spectroscopy and the airborne visible/infrared imaging spectrometer (aviris)," *Remote sensing of environment*, vol. 65, no. 3, pp. 227–248, 1998.
- [53] M. Story and R. G. Congalton, "Accuracy assessment: a users perspective," *Photogrammetric Engineering and remote sensing*, vol. 52, no. 3, pp. 397–399, 1986.
- [54] D. G. Altman and J. M. Bland, "Diagnostic tests. 1: Sensitivity and specificity," *BMJ: British Medical Journal*, vol. 308, no. 6943, p. 1552, 1994.
- [55] H. C. Kraemer, "Kappa coefficient," *Wiley StatsRef: Statistics Reference Online*, pp. 1–4, 2014.
- [56] J. Delegido, J. Verrelst, L. Alonso, and J. Moreno, "Evaluation of sentinel-2 red-edge bands for empirical estimation of green lai and chlorophyll content," *Sensors*, vol. 11, no. 7, pp. 7063–7081, 2011.